

1-1-2012

Dissipative Forces in the eElectrowetted Cassie-Wenzel Transition on Hydrophobic Rough Surfaces

C. P. Migliaccio
Purdue University

S. V. Garimella
Purdue University

Follow this and additional works at: <http://docs.lib.purdue.edu/coolingpubs>

Migliaccio, C. P. and Garimella, S. V., "Dissipative Forces in the eElectrowetted Cassie-Wenzel Transition on Hydrophobic Rough Surfaces" (2012). *CTRC Research Publications*. Paper 179.
<http://docs.lib.purdue.edu/coolingpubs/179>

This document has been made available through Purdue e-Pubs, a service of the Purdue University Libraries. Please contact epubs@purdue.edu for additional information.

DISSIPATIVE FORCES IN THE ELECTROWETTED CASSIE-WENZEL TRANSITION ON HYDROPHOBIC ROUGH SURFACES

Christopher P. Migliaccio and Suresh V. Garimella

*School of Mechanical Engineering and Birck Nanotechnology Center,
Purdue University, West Lafayette, Indiana*

Dissipative forces in the electrowetting-induced Cassie-Wenzel transition on hydrophobic rough surfaces are explored. High-speed imaging of droplet shape evolution during the electrically induced spreading process allows for the location of the contact line to be tracked as a function of time. A surface energy analysis quantifies the total energy dissipated via nonconservative forces during the spreading process. Though identified as the dominant dissipative effect in droplet spreading on smooth surfaces, contact line friction is shown to have a relatively weak influence on the spreading on rough surfaces. Supplemental files are available for this article. Go to the publisher's online edition of Nanoscale and Microscale Thermophysical Engineering to view the free supplemental file.

KEY WORDS: electrowetting, Cassie-Wenzel transition, contact-line friction, Dissipative forces, surface energy

INTRODUCTION

Electrowetting (EW) [1] on structured superhydrophobic surfaces [2, 3] is a promising droplet manipulation technique with potential microfluidic and heat transfer applications. EW in this setting is typically used to transition a droplet between the two wetting extremes—the Cassie state [4], where the droplet rests on top of the roughness elements of the surface (and on the air in the interelement spaces), and the Wenzel state [5], where the droplet wets, and is in intimate contact with, the roughness elements. In most cases, once the Wenzel state is achieved, the Cassie state cannot be recovered [2]; thus, practical applications are currently limited. Recent efforts [6–9] have focused on developing methods to overcome the dissipative forces [10] and energy barriers [10, 11] that hinder a complete Wenzel-Cassie reverse transition.

Methods to reduce the influence of dissipative forces in the electrical actuation of droplets have been explored [12–15]. The effective frictional force arising from molecular adsorption and desorption processes around the contact line is thought to be the dominant

Manuscript received 6 November 2011; accepted 5 April 2012.

The authors acknowledge financial support for this work from the Cooling Technologies Research Center, a National Science Foundation Industry/University Cooperative Research Center at Purdue University. Vaibhav Bahadur provided helpful feedback and suggestions regarding this work. The SEM images were obtained by Christopher Meyer.

Address correspondence to Suresh V. Garimella, School of Mechanical Engineering and Birck Nanotechnology Center, 585 Purdue Mall, Purdue University, West Lafayette, IN 47907. E-mail: sureshg@purdue.edu

NOMENCLATURE

<p>A interfacial area</p> <p>A^* pillar tip area</p> <p>a pillar width</p> <p>a_d pillar diagonal</p> <p>b pillar pitch</p> <p>c chord length</p> <p>E energy</p> <p>E' energy per unit length of wetting line</p> <p>F'_{CL} contact line friction force per unit length of wetting line</p> <p>h pillar height</p> <p>l length defined in Eq. (A1)</p> <p>P pillar perimeter</p> <p>R_{max} maximum radius</p> <p>R_{wet} wetted radius</p> <p>r_m ratio of total surface area (pillars and base) to footprint area</p> <p>U_{CL} contact line velocity</p> <p>V electrowetting voltage</p> <p>x radial coordinate</p> <p>Greek Symbols</p> <p>α central angle</p>	<p>γ interfacial energy</p> <p>$\Delta\theta$ contact angle hysteresis</p> <p>θ_0 static contact angle</p> <p>ξ contact line friction factor</p> <p>ϕ ratio of pillar tip surface area to footprint area</p> <p>Subscripts</p> <p>C Cassie state</p> <p>cap capacitive</p> <p>CL contact line</p> <p>EW electrowetted state</p> <p>LA liquid–air</p> <p>loss dissipative loss</p> <p>SA solid–air</p> <p>SL solid–liquid</p> <p>W Wenzel state</p> <p>0 state at the instant electrowetting voltage is applied</p> <p>Symbols</p> <p>\forall volume</p>
---	---

dissipative effect in the actuation of liquids on smooth surfaces [16–19]. Quantitative estimates of contact line friction have generally relied on the description of Blake and Haynes [20], who proposed a linearly proportional relationship between friction associated with these molecular processes and the contact line velocity; that is,

$$F_{CL}' = \xi U_{CL} \quad (1)$$

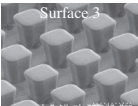
where F_{CL}' is the contact line friction force per unit length of the wetting line, ξ is the friction factor (N s/m^2), and U_{CL} is the velocity of the contact line. This expression has been used in various modeling efforts [17, 18, 21–23] to determine the value of ξ based on experimental observations of liquids spreading on smooth surfaces.

The energy dissipated due to nonconservative forces during a Cassie-Wenzel transition has not been experimentally quantified to date, to the best of the authors' knowledge. In this article, we quantify the dissipative effects and determine the role of contact line friction in EW-induced spreading on a variety of highly hydrophobic surfaces with engineered roughness elements under a range of actuation voltages. The findings from this work will further the design and modeling of superhydrophobic surfaces.

EXPERIMENTAL SETUP AND PROCEDURES

Cleanroom-grade deionized (DI) water droplets with an electrical resistivity of $1.80 \pm 0.02 \text{ M}\Omega \text{ cm}$ (four-wire method; model 34411A, Agilent, Englewood, CO) were used in the experiments. The laboratory environment was maintained at $21.0 \pm 0.3^\circ\text{C}$ at $30 \pm 2\%$ relative humidity. Highly doped silicon wafers with a dielectric layer of $1 \mu\text{m}$

Table 1 Pillar geometry, roughness parameters, static contact angles, and actuation voltages of the surfaces tested. Pillar dimensions were chosen such that some surfaces would have similar ϕ or r_m while having different h , a , and b . SEM images of select test surfaces are included in the final column. The measurement uncertainty in pillar geometry was $\pm 0.06 \mu\text{m}$

Surface	h, a, a_d, b (μm)	ϕ, r_m	θ_0 ($^\circ$)	Actuation voltages (V)	Representative SEM images
0	n/a, smooth	1, 1	113 ± 1	200	
1	11, 20, 28, 31	0.43, 1.93	138 ± 4	100, 200, 400	
2	11, 20, 28, 25	0.66, 2.42	135 ± 3	200, 400	
3	24, 21, 25, 40	0.26, 2.10	147 ± 3	200, 400	
4	24, 22, 24, 31	0.44, 2.81	139 ± 2	200, 400	
5	39, 22, 23, 57	0.13, 1.87	145 ± 2	400	
6	39, 23, 24, 40	0.28, 2.83	142 ± 2	400	
7	39, 24, 25, 31	0.49, 4.13	125 ± 6	400	

thermally grown oxide served as the substrates. SU-8 negative photoresist (MicroChem Corp., Newton, MA) was spin-coated and patterned using standard lithography processes to yield arrays of square pillars. The taller pillars exhibited some rounding of the vertical edges and a negative taper from the tip to the base due to imperfect contact during exposure (see Table 1). A scanning white-light interferometer (New View 6200, Zygo, Inc., Middlefield, CT) with a $50\times$ Mirau objective was used to accurately assess the pillar shapes (measurement uncertainty $\pm 0.06 \mu\text{m}$). By measuring the pillar width a and diagonal a_d (see Appendix), the pillar tip area A^* and perimeter P may be calculated (uncertainty $< 1\%$). The ratio a/a_d is a measure of pillar roundness (i.e., $a/a_d = 1/\sqrt{2}$ for square pillars and $a/a_d = 1$ for circular pillars). A thin, conformal coating of Teflon (AF 1600, DuPont, Wilmington, DE; 1% by weight in 3M FC-77, spun at 1,500 rpm for 30 s, baked at 95°C for 45 min) rendered the surface hydrophobic. An additional wafer was prepared with identical oxide and Teflon layers—but without SU-8 pillars—to serve as a smooth surface reference. Table 1 lists the pillar height h , width a , diagonal a_d , and pitch b of the surfaces tested, along with the dimensionless roughness parameters ϕ and r_m and the initial contact angle of DI water on the surfaces, θ_0 , as measured by an automated goniometer (model 590, Ramé-Hart Instrument Co., Succasunna, NJ). ϕ is the ratio of the total pillar tip surface area to the total footprint area of the substrate (i.e., $\phi = A^*/b^2$), and r_m is the ratio of the total surface area (including the tips and sidewalls of the pillars and the exposed base) to the total footprint area (i.e., $r_m = 1 + Ph/b^2$).

Rough surfaces are also characterized by the contact angle hysteresis $\Delta\theta$ [24], which is the difference between the advancing and receding contact angles of droplets. For pillared surfaces, the hysteresis is dependent on the droplet state—Cassie or Wenzel—and is related to the roughness parameters, with hysteresis in the Cassie state being a function of ϕ and hysteresis in the Wenzel state being a function of r_m [25]. Figure 1 presents the measured contact angle hysteresis for the surfaces in this work. The hysteresis for the reference smooth surface was $9 \pm 1^\circ$.

A schematic diagram of the test setup is shown in Figure 2. A droplet of DI water (average volume $1.6 \mu\text{L}$, standard deviation $0.8 \mu\text{L}$) was gently deposited on the test surface using a syringe. The dynamics of the droplet deposition were not considered in this

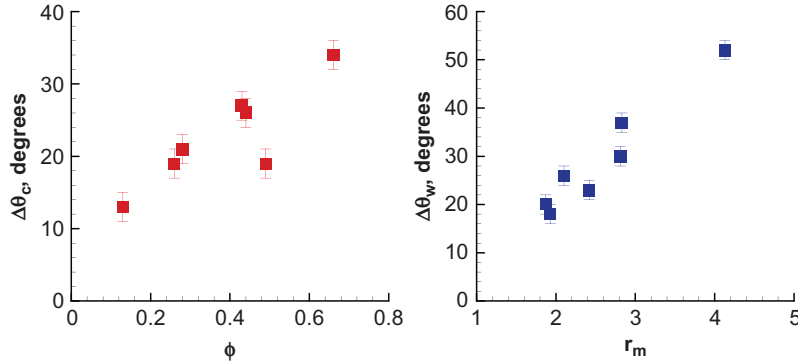


Figure 1 Measured contact angle hysteresis in the Cassie and Wenzel states for the rough surfaces tested (color figure available online).

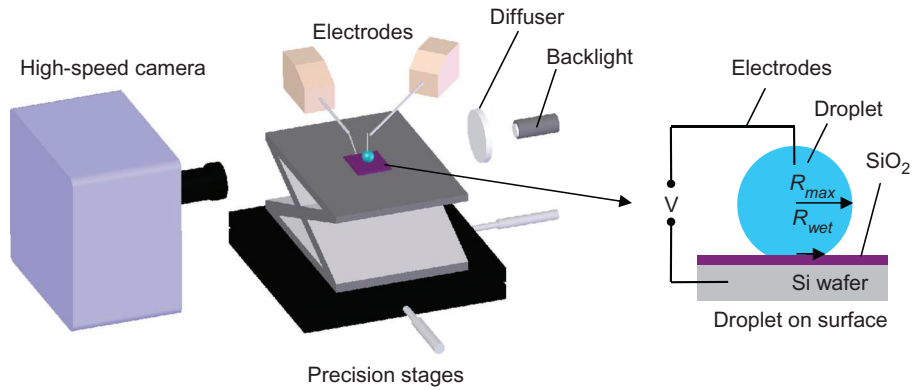


Figure 2 Schematic diagram of the test setup. The electrowetting voltage bias is applied between a wire electrode inserted into the droplet and an electrode contacting the silicon substrate (color figure available online).

work; rather, the displacement of the contact line during an EW-induced Cassie-Wenzel transition was investigated. Droplets in this study were much smaller than the capillary length (2.7 mm for water) and hence flattening of the droplets by gravity was neglected. The droplets took on a spherical cap shape on the surface; the volume was determined from optical measurements (resolution 7.7 μm/pixel) by

$$V = \frac{4}{3} \pi R_{\max}^3 - \frac{1}{6} \pi (R_{\max} (1 - \sin \theta_0)) (3R_{\text{wet}}^2 + (R_{\max} (1 - \sin \theta_0))^2) \quad (2)$$

where R_{\max} and R_{wet} are the maximum and wetted radii, respectively (see Figure 2). The uncertainty in the volume calculations was <1%.

All droplets were initially in the Cassie or “rolling ball” [26] state, as evidenced by the ease with which they could be dragged along the top of the pillars or blown off with a gentle stream of nitrogen gas. Moulinet and Bartolo [27] showed that droplets evaporating from superhydrophobic surfaces can gradually transition from the Cassie state to the Wenzel state by way of the partial impalement regime, where the droplet bottom interface sags and slowly moves down the pillar sidewalls. In the present work, the time

from deposition to electrical actuation was on the order of seconds; therefore, the partially impaled droplet state was avoided. Voltage bias was applied using a high-voltage power supply between a 125- μm -diameter chrome wire electrode inserted into the droplet and an electrode contacting the backside of the silicon substrate. The voltage required to trigger a Cassie-Wenzel transition is dependent on the dielectric properties of the test surface, physical properties of the liquid, and the equilibrium contact angle of the liquid on the reference smooth surface [28]. The observed transition voltages for the test surfaces ranged from ~ 75 to 200 V; surfaces with taller pillars required higher voltages. Voltage in excess of that required to trigger a Cassie-Wenzel transition was applied to guarantee that the Wenzel state was achieved (see Table 1). The transition was recorded by a high-speed camera (Photron Fastcam Ultima APX, San Diego, CA) at 10,000 frames per second. Figure 3 presents the Cassie-Wenzel transition of a droplet on surface 5 under an EW voltage of 400 V. The Wenzel state was realized ~ 1 ms after application of the actuation voltage; the contact line then moved in the radial direction, advancing through the pillars until the EW-induced spreading ceased.

RESULTS AND DISCUSSION

Figure 4a shows representative images during the shape evolution of a droplet on surface 1 at an EW voltage of 400 V. The contact line of the droplet (on both sides) was tracked as a function of time, and the displacement from its initial position was recorded. Figure 4b shows the contact line displacement for surface 1 at three applied EW voltages; corresponding movie files are available as supplementary material [29]. Higher voltages

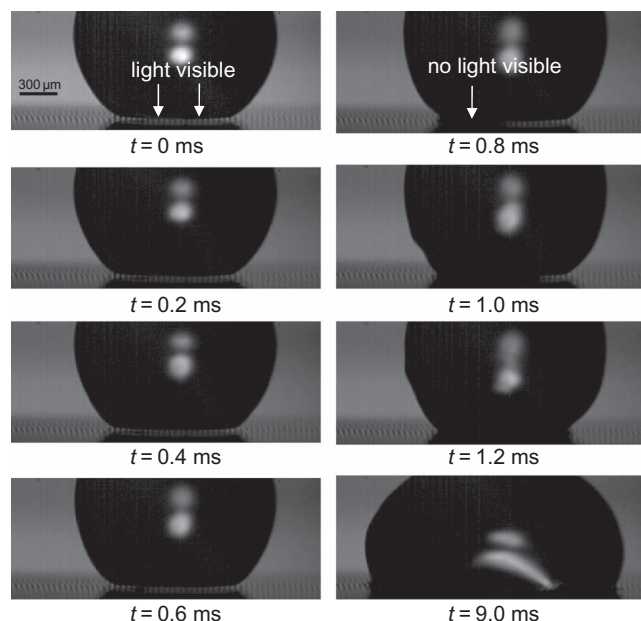


Figure 3 Electrowetting-induced Cassie-Wenzel transition of a 2.3- μL water droplet on surface 5 under an EW voltage of 400 V. Light is visible in the pillar interstices because surface 5 has relatively tall (39 μm) pillars and low ϕ (0.13). Our setup did not allow for light in the pillar interstices to be observed in other cases.

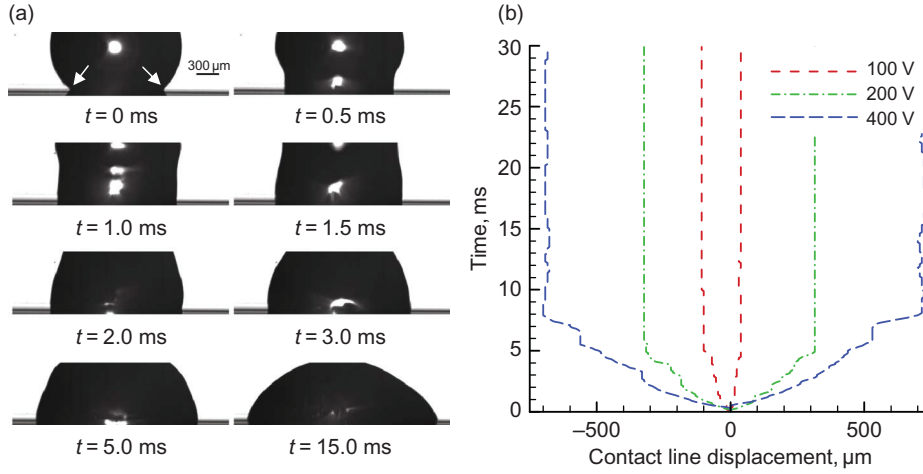


Figure 4 (a) Droplet shape evolution of a 2.4- μL water droplet during electrowetting-induced spreading on surface 1 at 400 V. The contact line (noted by arrows in the first pane) on both sides of the droplet was tracked through time. (b) Displacement of the contact lines during the spreading process relative to the initial position, 0, for water droplets on surface 1 at electrowetting voltages of 100, 200, and 400 V. Higher actuation voltages resulted in higher contact line velocities, as evidenced by the slope of the displacement vs. time plot. The uncertainty in position was $\pm 3.8 \mu\text{m}$ (color figure available online).

led to larger contact line displacements and higher contact line velocities (ranging from 1 to 10 cm/s in this work). Stick–slip behavior [30], where the contact line is periodically pinned and then slips between adjacent rows of pillars, was observed in the spreading process. Other nonconservative effects such as contact line friction [16, 17], hysteresis effects [31], and viscous shear [32] at the solid–liquid interface of the wetted base and pillars retarded the spreading process and dissipated energy from the system.

The total energy dissipated during the EW-induced Cassie–Wenzel transition was found by analyzing the droplet shape before and after the transition. Initially, the droplet was in the Cassie state; at the instant the EW voltage V was applied, the surface energy is given as

$$E_{C,0} = [A_{LA} + A_{SL} (1 - \phi)] \gamma_{LA} + \phi A_{SL} (\gamma_{SL} - \gamma_{SA}) - E_{C,\text{cap}} \quad (3)$$

where A and γ are the interfacial area and energy, respectively, and $E_{C,\text{cap}}$ is the effective reduction in interfacial energy due to capacitive energy storage in the dielectric layer during EW [1]. The subscripts LA, SL, and SA distinguish between the liquid–air, solid–liquid, and solid–air interfaces, respectively. The application of the EW voltage triggers a transition to the Wenzel state and subsequent radial motion of the contact line. The total surface energy of a droplet in the electrowetted Wenzel state after the EW-induced spreading has ceased (i.e., the contact line motion has stopped) is then expressed as

$$E_{W,\text{EW}} = A_{LA} \gamma_{LA} + \phi A_{SL} (\gamma_{SL} - \gamma_{SA}) + (1 - \phi) A_{SL} (\gamma_{SL} - \gamma_{SA}) \\ + (r_m - 1) A_{SL} (\gamma_{SL} - \gamma_{SA}) - E_{W,\text{cap}} \quad (4)$$

where $E_{W,\text{cap}}$ is the interfacial energy reduction during EW when the droplet is in the Wenzel state. The nonuniform thickness and dissimilar materials (SU-8, SiO_2 , and—when

the droplet is in the Cassie state—air) of the dielectric layer complicate analytical modeling of the capacitive energy storage of the surfaces [28]; hence, the energies $E_{C,\text{cap}}$ and $E_{W,\text{cap}}$ were determined by modeling 3D unit cells of each surface and actuation voltage using COMSOL Multiphysics software [33]. Because a DC voltage bias is used in this work, the liquid behaved as a perfect conductor [34]; thus, the voltage boundary condition was applied between the silicon substrate and the SL interface for the Wenzel state cases and between the silicon substrate and composite SL-LA interface for the Cassie state cases.

The total energy lost due to dissipative effects E_{loss} is equal to the difference between Eqs. (3) and (4). The energy dissipated due to the effective friction of the molecular displacement process at the contact line [20], E_{CL} , is found by integrating the friction force around the contact line and over the distance it moves during the EW-induced spreading:

$$E_{\text{CL}} = 2\pi r_m \int_{x_0}^{x_{\text{EW}}} F_{\text{CL}}' x dx = 2\pi r_m \int_{x_0}^{x_{\text{EW}}} \xi U_{\text{CL}} x dx \quad (5)$$

where x is the radial coordinate of the contact line and the subscripts 0 and EW denote the location of the contact line initially (at the instant the EW voltage is applied) and after the EW-induced spreading has ceased, respectively. It is clear that as the contact line moves over pillared areas of the substrate, the contact line length is extended due to wetting of the pillar sidewalls, thus making the case at hand more complex than spreading on a smooth surface. The enhanced wetted surface area increases the magnitude of the effective friction at the contact line; however, the extent of increase is difficult to quantify because the contact line extension varies with position on the surface. In this work, we modified the contact line length by the roughness parameter r_m to account for the enhanced wetted surface area. The friction factor ξ was found by recording the spreading process of a droplet under EW bias on the smooth reference surface. Assuming that contact line friction dominates in this smooth surface case [16–18], E_{CL} was equated to E_{loss} , yielding a friction factor of 0.39 N s/m^2 . Wang and Jones [18] previously reported a friction factor range of $\sim 0.2\text{--}0.6 \text{ N s/m}^2$ for DI water on a smooth surface under DC actuation. Past investigations [18, 21] reported little or no dependence of ξ on EW voltage; therefore, ξ is assumed to be independent of voltage in this work, and we set $\xi = 0.39 \text{ N s/m}^2$ in the analysis of the results.

Because droplet volumes between runs were not identical ($1.6 \pm 0.8 \mu\text{L}$), the energy lost to nonconservative forces was considered on a per change in contact line length basis; that is, $E'_{\text{loss}} = E_{\text{loss}} / [2\pi (x_{\text{EW}} - x_0)]$, to allow for an unbiased comparison. Figure 5 shows E'_{loss} and E'_{CL} as a function of the surface roughness parameter r_m at the different EW voltages applied. The solid lines represent the average energy lost to contact line friction forces for each EW voltage level (i.e., E_{CL} calculated as discussed above). Contact line friction accounted for an average of approximately 30 and 10% of total energy dissipated for the 100 and 400 V runs, respectively. This is in stark contrast to the dominant role that contact line friction forces are reported to play in the spreading process on smooth surfaces [16–18]. At higher actuation voltages, the degree of spreading is enhanced, so that dissipative effects related to the number of pillars encountered, such as viscous drag forces and stick–slip of the contact line, become more pronounced. Delineating the respective individual roles of these other effects and determining the appropriate approach to describe the contact line as it spreads through the elements of a rough surface will require additional experimental and modeling efforts.

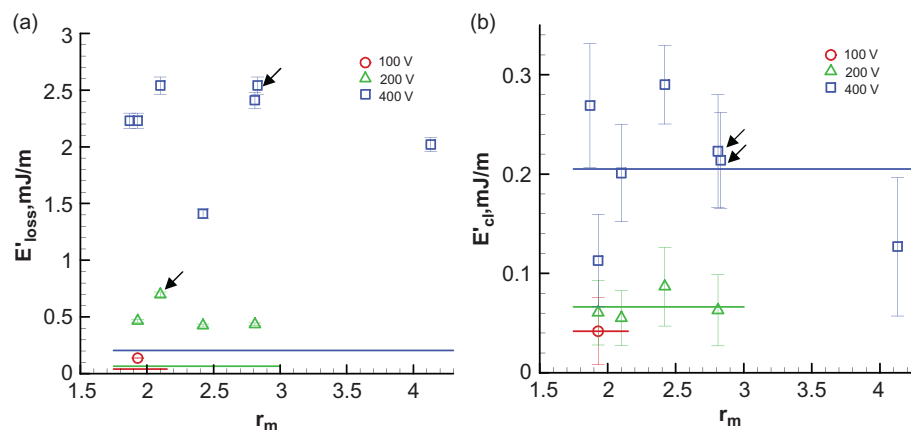


Figure 5 (a) Total dissipative energy losses per change in contact line length as a function of surface roughness r_m at different actuation voltages. (b) Estimated energy losses due to contact line friction forces per change in contact line length as a function of surface roughness r_m at different actuation voltages. In (a) and (b), symbols represent the average of three data points for each test condition. The standard deviation of the three data points for each test condition was generally between 5 and 25%, except for the cases noted by black arrows (standard deviation $\sim 40\%$). Error bars represent the propagated uncertainty due to measured quantities. Because E'_{CL} is a function of contact line velocity, uncertainty was dominated by measurement resolution of contact line position ($\pm 3.8 \mu\text{m}$) and time ($\pm 0.05 \text{ ms}$). The solid lines represent the average estimated energy losses due to contact line friction forces at each actuation voltage (color figure available online).

CONCLUSIONS

This article reports on the use of surface energy analysis to quantify dissipative effects in Cassie-Wenzel transition experiments with droplets on structured roughness hydrophobic surfaces. Unlike past investigations on smooth surfaces, molecular-level contact line friction forces are shown to have relatively weak influence on spreading processes on rough surfaces. Other dissipative effects amplified by the presence of the roughness elements such as viscous shear forces and stick-slip of the contact line were identified from experimental measurements as being important in this work. These findings will prove useful in the design of superhydrophobic surfaces and foster the development of new applications.

REFERENCES

1. F. Mugele and J.-C. Baret, Electrowetting: From Basics to Applications, *Journal of Physics: Condensed Matter*, Vol. 17, pp. R705–R774, 2005.
2. J. Heikenfeld and M. Dhindsa, Electrowetting on Superhydrophobic Surfaces: Present Status and Prospects, *Journal of Adhesion Science and Technology*, Vol. 22, pp. 319–334, 2008.
3. A. Ahuja, J.A. Taylor, V. Lifton, A.A. Sidorenko, T.R. Salamon, E.J. Lobaton, P. Kolodner, and T.N. Krupenkin, Nanonails: A Simple Geometrical Approach to Electrically Tunable Superhydrophobic Surfaces, *Langmuir*, Vol. 24, pp. 9–14, 2008.
4. A.B.D. Cassie and S. Baxter, Wettability of Porous Surfaces, *Transactions of the Faraday Society*, Vol. 40, pp. 546–551, 1944.
5. T.N. Wenzel, Surface Roughness and Contact Angle, *Journal of Physical Chemistry*, Vol. 53, pp. 1466–1467, 1949.

6. T.N. Krupenkin, J.A. Taylor, E.N. Wang, P. Kolodner, M. Hodes, and T.R. Salamon, Reversible Wetting–Dewetting Transitions on Electrically Tunable Superhydrophobic Nanostructured Surfaces, *Langmuir*, Vol. 23, pp. 9128–9133, 2007.
7. M.S. Dhindsa, N.R. Smith, J. Heikenfeld, R.D. Rack, J.D. Fowlkes, M.J. Doktycz, A.V. Melechko, and M.L. Simpson, Reversible Electrowetting of Vertically Aligned Superhydrophobic Carbon Nanofibers, *Langmuir*, Vol. 22, pp. 9030–9034, 2006.
8. J.B. Boreyko and C.-H. Chen, Restoring Superhydrophobicity of Lotus Leaves with Vibration-Induced Dewetting, *Physical Review Letters*, Vol. 103, p. 174502, 2009.
9. N. Kumari and S.V. Garimella, Electrowetting-Induced Dewetting Transitions on Superhydrophobic Surfaces, *Langmuir*, Vol. 27, pp. 10342–10346, 2011.
10. V. Bahadur and S.V. Garimella, Electrowetting-Based Control of Droplet Transition and Morphology on Artificially Microstructured Surfaces, *Langmuir*, Vol. 24, pp. 8338–8345, 2008.
11. B. He, N.A. Patankar, and J. Lee, Multiple Equilibrium Droplet Shapes and Design Criterion for Rough Hydrophobic Surfaces, *Langmuir*, Vol. 19, pp. 4999–5003, 2003.
12. J.S. Kuo, P. Spicar-Mihalic, I. Rodriguez, and D.T. Chiu, Electrowetting-Induced Droplet Movement in an Immiscible Medium, *Langmuir*, Vol. 19, pp. 250–255, 2003.
13. A. Torkkeli, J. Saarihahti, A. Haara, H. Harma, T. Soukka, and P. Tolonen, Electrostatic Transportation of Water Droplets on Superhydrophobic Surfaces, *Proceedings - IEEE International Conference on Micro Electro Mechanical Systems*, Vol. 1, pp. 475–478, 2001.
14. P. Paik, V.K. Pamula, and K. Chakrabarty, Thermal Effects on Droplet Transport in Digital Microfluidics with Applications to Chip Cooling, *Proceedings of the Intersociety Conference—Thermomechanical Phenomena in Electronic Systems*, Vol. 1, pp. 649–654, 2004.
15. C.G. Cooney, C.-Y. Chen, M.R. Emerling, A. Nadim, and J.D. Sterling, Electrowetting Droplet Microfluidics on a Single Planar Surface, *Microfluidics and Nanofluidics*, Vol. 2, pp. 435–446, 2006.
16. V. Bahadur and S.V. Garimella, An Energy-Based Model for Electrowetting-Induced Droplet Actuation, *Journal of Micromechanics and Microengineering*, Vol. 16, pp. 1494–1503, 2006.
17. H. Ren, R.B. Fair, M.G. Pollack, and E.J. Shaughnessy, Dynamics of Electro-Wetting Droplet Transport, *Sensors and Actuators, B: Chemical*, Vol. 87, pp. 201–206, 2002.
18. K.-L. Wang and T.B. Jones, Electrowetting Dynamics of Microfluidic Actuation, *Langmuir*, Vol. 21, pp. 4211–4217, 2005.
19. J.M. Oh, S.H. Ko, and K.H. Kang, Analysis of Electrowetting-Driven Spreading of a Drop in Air, *Physics of Fluids*, Vol. 22, p. 032002, 2010.
20. T.D. Blake and J.M. Haynes, Kinetics of Liquid/Liquid Displacement, *Journal of Colloid and Interface Science*, Vol. 30, pp. 421–423, 1969.
21. C. Decamps and J. De Coninck, Dynamics of Spontaneous Spreading under Electrowetting Conditions, *Langmuir*, Vol. 16, pp. 10150–10153, 2000.
22. A. Hamraoui, K. Thuresson, T. Nylander, and V. Yaminsky, Can a Dynamic Contact Angle Be Understood in Terms of a Friction Coefficient? *Journal of Colloid and Interface Science*, Vol. 226, pp. 199–204, 2000.
23. J.H. Chen and W.H. Hsieh, Electrowetting-Induced Capillary Flow in a Parallel-Plate Channel, *Journal of Colloid and Interface Science*, Vol. 296, pp. 276–283, 2006.
24. J.F. Joanny and P.-G. de Gennes, A Model for Contact Angle Hysteresis, *Journal of Chemical Physics*, Vol. 81, pp. 552–562, 1984.
25. K.-Y. Yeh and L.J. Chen, Contact Angle Hysteresis on Regular Pillar-Like Hydrophobic Surfaces, *Langmuir*, Vol. 24, pp. 245–251, 2008.
26. T.N. Krupenkin, J.A. Taylor, T.M. Schneider, and S. Yang, From Rolling Ball to Complete Wetting: The Dynamic Tuning of Liquids on Nanostructured Surfaces, *Langmuir*, Vol. 20, pp. 3824–3827, 2004.

27. S. Moulinet and D. Bartolo, Life and Death of a Fakir Droplet: Impalement Transitions on Superhydrophobic Surfaces, *European Physical Journal E*, Vol. 24, pp. 251–260, 2007.
28. V. Bahadur and S.V. Garimella, Electrowetting-Based Control of Static Droplet States on Rough Surfaces, *Langmuir*, Vol. 23, pp. 4918–4924, 2007.
29. Please see online supplementary materials.
30. P.S.H. Forsberg, C. Priest, M. Brinkmann, R. Sedev, and J. Ralston, Contact Line Pinning on Microstructured Surfaces for Liquids in the Wenzel State, *Langmuir*, Vol. 26, pp. 860–865, 2009.
31. S.W. Walker, B. Shapiro, and R.H. Nochetto, Electrowetting with Contact Line Pinning: Computational Modeling and Comparisons with Experiments, *Physics of Fluids*, Vol. 21, p. 102103, 2009.
32. R. Weiqing and E. Weinan, Boundary Conditions for the Moving Contact Line Problem, *Physics of Fluids*, Vol. 19, p. 022101, 2007.
33. COMSOL AB, *COMSOL Multiphysics 3.3 User's Guide*, COSMOL, Inc. Burlington, MA, 2006.
34. J.S. Hong, S.H. Do, K.H. Kang, I.S. Kang, A Numerical Investigation on AC Electrowetting of a Droplet, *Microfluidics Nanofluidics*, Vol. 5, pp. 263–271, 2008.

APPENDIX A: PILLAR SHAPE ASSESSMENT

Accurate assessment of pillar shapes is crucial in the calculation of the dimensionless roughness parameters ϕ and r_m . The taller pillars in this work exhibited some rounding of the vertical edges (see Table 1). By measuring the pillar width a and diagonal a_d and taking the rounded vertical edges of the pillars to be an arc, the length l (see Figure A1) is given by

$$l = \sqrt{\left(\frac{a_d}{2}\right)^2 - \left(\frac{a}{2}\right)^2} \quad (\text{A1})$$

The chord length c and central angle α are then

$$c = \sqrt{2} \left(\frac{a}{2} - l\right) \quad (\text{A2})$$

$$\alpha = 2 \sin^{-1} \left(\frac{c/2}{a_d/2}\right) \quad (\text{A3})$$

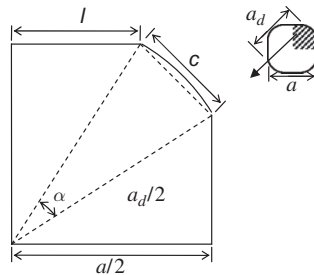


Figure A1 Plan view of a pillar tip showing the two measured dimensions a and a_d with the quadrant used for the calculations. Taking the rounded corner of the pillar to be an arc, the pillar tip area and perimeter were calculated.

The pillar tip area A^* and perimeter P may then be calculated as

$$A^* = 4 \left(\frac{a}{2} l + \left(\frac{a_d}{2} \right)^2 \frac{\alpha}{2} \right) \quad (\text{A4})$$

$$P = 4 \left(2l + \frac{a_d}{2} \alpha \right) \quad (\text{A5})$$

By accounting for the actual pillar shape in this way, significant errors (up to $\sim 20\%$ for surface 7) in the calculation of ϕ and r_m that would be introduced by assuming the pillar shapes to be square are avoided.